Geochemical Perspectives Letters

Variable $\delta^{11}B$ signatures reflect dynamic evolution of the Mariana serpentinite forearc

E. Cannaò, B. Debret

Supplementary Information

The Supplementary Information includes:

- Analytical Methods
- Background Geochemical Data
- Geochemical Modelling
- Tables S-1 to S-7
- Figures S-1 to S-9
- Supplementary Information References

Analytical Methods

In situ trace element determination

The *in situ* trace element compositions of rock-forming minerals (serpentine and brucite) and mineral relicts (olivine and orthopyroxene) were determined using a laser ablation microprobe system (Analyte Excite 193nm ArF excimer, Teledyne Photon Machines) coupled with a single-collector quadrupole inductively coupled plasma mass spectrometer (ICP-MS) iCAP-RQ (Thermo Fisher Scientific) hosted at the Geochemistry, Geochronology and Isotope Geology Laboratory at the Dipartimento di Scienze della Terra "A. Desio", Università degli Studi di Milano (Italy). The laser ablation system is equipped with a double volume ablation cell (HelEx II) for fasting wash out. Ablated particles were transported to the ICP-MS using He gas at a flow rate of 0.52 and 0.35 L/min into the sample chamber and in the HelEx II cup, respectively. Laser spot size range from 40 to 65 µm for unknown and was fixed to 40 µm for standard glasses. A laser fluence of 3.0 J/cm^2 and repetition rate of 10 Hz were used for both standards and mineral unknown. Each spot was analysed for a total of 110 s: (i) 40 s of background analyses (laser off), which include 10 s of laser warm up, (ii) 60 s of laser ablation measuring isotope peak intensity followed by (iii) 10 s of wash out time. The synthetic basaltic glass GSD-2g (Wilson, 2018) was used as external standard, whereas ^{29}Si (for serpentine, olivine, orthopyroxene) and ^{25}Mg (for brucite) were used as internal standards. Quality control was achieved analysing as unknown in each analytical run the andesitic glass ARM3 (Wu *et al.*, 2019) and the USGS reference basaltic glass BCR-2g (GeoReM database). Precision is often better than 10 % and accuracy is within 15 % of the preferred values for most of the elements.

In situ B isotope determination

The *in situ* B isotope compositions of serpentines have been measured using the same laser microprobe system used for the determination of trace element connected to a double focusing multi-collector (MC-)ICP-MS, Neptune *XT* (Thermo Fisher Scientific) installed at the Geochemistry, Geochronology and Isotope Geology Laboratory at the Dipartimento di Scienze della Terra "A. Desio", Università degli Studi di Milano (Italy). The laser ablation system was operated in single spot mode with a laser fluence of 3.5 J/cm^2, repetition rate of 10 Hz and fixed spot size of 85 µm in diameter. These

laser parameters were kept constant for both standards and serpentine unknown to minimise potential isotope fractionation (Kimura *et al.*, 2016). Ablation was carried out under He flux at flow rate of 0.51 L/min and 0.24 L/min into the sample chamber and in the HelEx II arm, respectively. Nitrogen gas was used as additional gas at a flow rate of *ca.* 5 mL/min and added downstream of the ablation cell in order to improve the sensitivity. The Neptune *XT* was operated in low resolution mode, using Ni Jet-sample and X-skimmer cones to improve the sensitivity. The ^{11}B and ^{10}B ion beam were measured in H4 and L2, respectively, using Faraday cup detector system both equipped with 10^{13} Ω resistors, thus ensuring an optimal signal/noise ratio. The tau correction was applied before data are exported. The radio frequency of the ICP torch was set to 1000 W. The system was tuned daily by ablating the NIST SRM612 synthetic glass (B content *ca.* 35 µg/g; Jochum *et al.*, 2011) with a spot size of 40 µm at a rate of 10 Hz and a laser fluence of 6.0 J/cm^2, resulting in a mean sensitivity on ^{11}B of at least 1.0 mV/µg/g. The signal measured (tens to hundreds of mV) for ^{10}B and ^{11}B, used to calculate the $^{11}B/^{10}B$ ratio, are corrected from instrument background that were below 0.10 and 0.50 mV, respectively. Each analyses comprises 156 cycles of 0.524 s integration time and each measurement included 30 s of background acquisition (laser off; comprising 10 s of laser warm up), 40 s of data acquisition followed by 8 s of was out time. Data treatment was made off-line, using an *in-house* spreadsheet. Ratios exceeding the 2 standard deviation (2 s.d.) of the mean have been regarded as outliers and discharged. Note that no downhole isotope ratio fractionation was observed. The analytical precision is commonly dependent upon the intensity of B signal, which is related to the B content of the analysed material. However, the relatively high 2 standard error (s.e.) shown by some analyses with high B content (*e.g.*, sample M12) is related to the small thickness of the available rock specimen in thin section.

The results are reported in the common delta(δ)-notation as permil (‰) and expressed relative to the isotopic ratio of the reference boric acid NIST SRM 951 ($^{11}B/^{10}B = 4.04362 \pm 0.00137$ 2 s.d.; Catanzaro *et al.*, 1970). Mass-bias fractionations were corrected using the standard-sample bracketing approach. A matrix-matching reference material, the Koh-ol olivine (Bouihol *et al.*, 2012; provided by C.J. De Hoog), was used as calibrating standard to avoid potential Ca-induced interference on the measured $^{11}B/^{10}B$ ratios (see Fietzke and Anagnostou, 2023, for details). This olivine has relatively homogeneous B isotope composition (−4.6 ± 0.8 ‰ 2 s.d.; Clarke *et al.*, 2020) but variable B content, ranging from 60 to 120 µg/g (Bouihol *et al.*, 2012; Cannaò *et al.*, 2024). Hereafter, the uncertainty of $\delta^{11}B$ data is reported as 2 s.d. for mean values and as 2 s.e. for single spot analyses. Quoted uncertainties are quadratic additions of the within run precision of each analysis and the reproducibility of the Koh-ol olivine during each analytical run, which range from 0.20 to 0.41 ‰ (2 s.d., $n = 9–15$; Table S-2). Estimated B concentrations were obtained by comparing the intensities of the unknown with that of the NIST SRM612 synthetic glass analysed within each runs. An in-house antigorite with *ca.* 16 µg/g of B and $\delta^{11}B$ of +22.3 ± 0.4 ‰ (sample MS VAR 10-01 in Cannaò *et al.*, 2016) was used to assess accuracy. The measured $\delta^{11}B$ range between +19.80 ± 0.78 and +22.68 ± 0.64 ‰ (2 s.e.; see Table S-3, Fig. S-1), with a mean of +21.41 ± 1.74 ‰ (2 s.d., $n = 10$) overlapping the $\delta^{11}B$ bulk value obtained with TIMS after chemical purification (Cannaò *et al.*, 2016). Our results indicate the lack of isotope fractionation due to matrix effects (*e.g.*, different water content between olivine and antigorite), signal intensities or instrumental bias, thus proving the high quality of the $\delta^{11}B$ data reported in this contribution. Further information about the analytical protocol can be found in Cannaò *et al.* (2024).

Background Geochemical Data

Chondrite-normalised (C1) rare earth element (REE) compositions of the serpentines for all samples (Fig. S-3) are depleted (from 0.002 to 0.5 times the C1) with mean La_N/Yb_N ratios ranging from 0.05 to 0.33, except for the blue-serpentine (La_N/Yb_N ratio of 1.41). Lizardite from samples M10, M12 and M20 show negative seawater-like Ce anomaly, which is slightly detected in atg-bearing samples. The REE pattern of the brucite from sample M20 overlap those of the coexisting serpentines. Primitive mantle-normalised trace element plots (Fig. S-4) show positive anomalies in several fluid-mobile (B, As, Sb) and redox-sensitive elements (*e.g.*, Mo). The low-*T* liz-bearing sample M10 and the antigorite in the transitional sample M12 also shown variable enrichments in Cs, W and Li, that are lacking in the atg-bearing samples (M15-M16). Brucite from sample M20 shows variable enrichments in Sr, Ba, Cs, Li, Mo, W and Pb. Antigorite from transitional sample M12 show the highest and variable As contents (from 0.360 to 19.0 µg/g) followed by the atg-bearing sample M16 (1.29 ± 1.16 µg/g). Strontium concentrations decrease from liz- to atg-bearing samples, in agreement with bulk data (Debret *et al.*, 2019). Of relevance are the correlations between W/Ba ratio and Ba and Sr contents of the serpentines, where lizardite have high Ba contents and low W/Ba ratios, in contrast to antigorite showing low Ba contents and high W/Ba ratios (Fig. S-5). The high Ba and Mo contents in lizardite from sample M10, result in low W/Ba and Mo/Ce ratios (Fig. 2c), supporting the higher mobility of Ba compared to W and the mobilisation of Mo

in aqueous fluids during the onset of slab devolatilisation (*e.g.*, König *et al.*, 2008; H.-Y. Li *et al.*, 2021). Evidence of Mo mobilisation at the Asùt Tesoru seamount has also been documented in near-surface pore water and resulted from microbially mediated dissolution of Mn oxyhydroxides (Hulme *et al.*, 2010). In the transitional sample M12, lizardite are characterised by higher As/Pb ratios than antigorite that positively correlate with W contents and W/Ba ratios Decreasing $\delta^{11}B$ signatures from liz- to atg-bearing samples is also associated with relatively enrichment in the W/Ba ratios (Fig. S-5).

In Table S-3 are also reported the trace element concentrations of primary mantle minerals, olivine and orthopyroxene. As expected, olivine is enriched in Ni and Co and depleted in Cr, V, Sc and Ti compared to orthopyroxene relicts. Some analyses show anomalous high enrichments in B (up to 6 µg/g) that are interpreted to be representative of minor amount of serpentine present within the primary phases, *e.g.*, minute serpentinised exsolution lamellae in orthopyroxene. Therefore, these data are not representative of the primary B inventory of the mantle phases.

Geochemical Modelling

Stable isotope systematics are sensitive to changes in the chemical-physical condition of a system and, particularly, B isotopes are strongly sensitive to variations in *T* and pH conditions. In solids and fluids, B occurs either in tetrahedral ([4]) or trigonal ([3]) coordination with O: ^{10}B prefers [4] coordination and ^{11}B the [3] one (Kakihana *et al.*, 1977). A relationship exists with B coordination and pH conditions: at low pH B is dominantly in trigonal coordination, whereas the tetrahedral coordination become dominant towards more alkaline conditions (Palmer and Swihart, 1996). This B speciation dominate the B isotope fractionation between coexisting phases at equilibrium conditions (first-order criteria) even though second-order effects must be considered (*e.g.*, Palmer *et al.*, 1992; Y.-C. Li *et al.*, 2021). For a detail and exhaustive review on B isotope fractionation, see Kowalski and Wunder (2018).

According to literature, B is [4]-coordinated in serpentine (Pabst *et al.*, 2011) and in clay minerals (Spivack and Edmond, 1987), whereas in olivine B is commonly incorporated in trigonal coordination (Ingrin *et al.*, 2014). More recently, Muir *et al.* (2022) suggested that B can be incorporated in olivine in tetrahedral coordination if B in olivine can be related to an H defect. If so, the B isotope fractionation in the hydrated ultramafic system is more complex than previously thought. For the purpose of this work, we assume that B is in [4]-coordinated in serpentine and mica and [3]-coordinated in olivine (no B isotope fractionation between olivine [4] and fluid [3]–[4] are reported yet). In the proposed models (see below), the coordination of B in the fluid phase ranges from pure acid condition (100–0 % [3]–[4]) to pure alkaline condition (0–100 % [3]–[4]). Mixed condition considering 50–50 % of $B_{[3]}$–$B_{[4]}$ is also reported.

Boron isotope composition of serpentines flushed by shallow and deep slab-derived fluids

Hereafter we calculated the possible effect of B isotope fractionation between serpentine and slab-derived fluids produced during the progressive dehydration of slab material using Rayleigh distillation equations following the approach proposed by Liu *et al.* (2022), which is based on the work of Rosner *et al.* (2003). This geochemical modelling provides a general understanding of the trend(s) in B isotope signatures of serpentines formed during interaction with slab-derived fluids. It should be noted that this approach is a simplification of a complex system and is not intended to provide a complete and exhaustive analysis of the entire system, for which further investigations are required.

We provided geochemical models using updated B isotope fractionation factors, testing different conditions in term of initial $\delta^{11}B$ of the slab material and pH condition of the system, with the latter strongly affecting the amplitude of the B isotope fractionation between solids and fluids. Being micas the main repository for B in altered oceanic crust (*e.g.*, Marschall *et al.*, 2007) and sedimentary sequences (besides tourmalines), the contribution of other phases were not considered. We used the mica-fluid B isotope fractionation of Kowalski *et al.* (2013) considering B speciation in fluid in both trigonal and tetrahedral coordination, reflecting acid/neutral *vs.* alkali conditions, respectively. We assumed that 80 % of the initial B was lost at 800 °C, and its release is assumed to be linear function with *T* (Rosner *et al.*, 2003). We used the available lizardite-fluid B isotope fractionation derived from the computational study of Li *et al.* (2022, B-lizardite-III_j structure), assuming B speciation in fluid is in both trigonal and tetrahedral coordination, consistently with the mica-fluid B isotope fractionation modelled. Three scenarios were considered with initial slab B contents and $\delta^{11}B$ signatures of 5.2 µg/g and +3.4 ‰ (Smith *et al.*, 1995), 3.6 µg/g and +7.9 ‰ (Yamaoka *et al.*, 2012), and 17 µg/g and +21.7 ‰ (McCaig *et al.*, 2018). The first two pairs of data are representative of the present-day/fossil altered oceanic crust (Smith *et al.*, 1995) and bulk oceanic crust now exposed in Oman (Yamaoka *et al.*, 2012), respectively. The last

pair of data is representative of lower gabbro section from the Hess Deep fast-spreading ocean (McCaig *et al.*, 2018). Data and results are reported in Table S-5 and Figure S-6.

As general trends, slab-derived fluids are always enriched in ^{11}B compared to initial slab compositions, and lizardite has always lower $\delta^{11}B$ signatures than the slab restite. This is mainly due to the higher fluid-solid B isotope fractionation of lizardite compared to mica (Li *et al.*, 2022), which is related to B/Si ordering in layered silicate minerals (Y.-C. Li *et al.*, 2021) and of second-order effects on B isotope fractionation (see Kowalski and Wunder, 2018, for details). Notably, at low T (<200 °C) the B isotope fractionation for lizardite is more pronounced than at middle T (200–500 °C), which become less T-dependent, particularly in acid/neutral system conditions. An interesting result from the modelling, and in contrast with common thoughts (*e.g.*, Benton *et al.*, 2001; Tonarini *et al.*, 2011), is that the $\delta^{11}B$ composition of lizardite increase with T – *i.e.* with prograde subduction – even if the B isotope fractionation between lizardite and fluid decreases.

Overall, the validity of the three proposed scenarios is supported by literature data on high-P mafic rocks – *i.e.* blueschists and eclogites as representative of the slab restite. In the first two cases (Fig. S-6a,b), negative $\delta^{11}B$ signatures of the slab restite evolve towards lower values during progressive dehydration, in agreement with the common negative $\delta^{11}B$ imprints of mafic high-P rocks experienced dehydration during progressive subduction (*e.g.*, Peacock and Hervig, 1999; Pabst *et al.*, 2012; Liu *et al.*, 2022). In the last case (Fig. S-6c) the $\delta^{11}B$ signatures of the slab restite is always enriched in the heavy B isotope (*i.e.* positive $\delta^{11}B$). The occurrence of high-P mafic rocks with positive $\delta^{11}B$ signatures have been recently documented in the Voltri Massif (up to +10 ‰ at *ca.* 550 °C and 2.4 GPa; see Cannaò *et al.*, 2023, for details).

Building upon the model parameters of Liu *et al.* (2022), if an initial $\delta^{11}B$ signature of the slab of +7.9 ‰ is assumed (Yamaoka *et al.*, 2012; Fig. S-6b), we obtained a good match for the slab restite and $\delta^{11}B$ signatures of metabasalts collected in the Asùt Tesoru, Fatangisña and South Chamorro seamounts (Liu *et al.*, 2022; Pabst *et al.*, 2012). The formation of lizardite and antigorite with variable $\delta^{11}B$ signatures from +20 to −5 ‰ can be achieved considering variable water/rock ratios at different T. Following the approach of Simon *et al.* (2016), reporting a dimensionless mass balance equations for a dynamic single-pass open system evolution, we calculated water/rock ratios (by weight) ranging from 5 to 90 (model parameters in Table S-6). The obtained water/rock ratios are consistent with the high fluid flux environment characterising the supra-subduction mantle in forearc regions. The calculation assumes B coordination in fluid is 50 % trigonal and 50 % tetrahedral, reflecting different degree of pH conditions as serpentinisation progress (*e.g.*, Seyfried and Dibble, 1980). Boron partition coefficient between rock and fluid (D_B) was fixed to 6, calculated following the approach of Foustoukos *et al.* (2008), which provides a broad correlation between pH and D_B. Figure S-7 reports the relationship between W/R ratios and $\delta^{11}B$-B (µg/g) of the reacted rock (*i.e.* serpentinites) at different D_B and considering 50–50 % of B in trigonal and tetrahedral coordination. The change in D_B from high (20) to low (3) values should be representative of the increasing T during serpentinisation progress (*e.g.*, Seyfried and Dibble, 1980) in subduction settings. The lowest the D_B, the lowest the B contents in the serpentines (Fig. S-7b). Calculations considering lower initial $\delta^{11}B$ signature of the slab (*e.g.*, +3.4 ‰; Smith *et al.*, 1995), variable B speciation in the fluid phase and B partition coefficient however do not significantly change the results of the model and the interpretation of the data (Fig. S-8).

Boron isotope composition of serpentines during phase transition

It has been proposed that if B is released during the prograde lizardite to antigorite phase transition in subduction settings, B isotope fractionation should occur (Cannaò, 2020, and references therein). If so, the newly formed high-P antigorite should be depleted in ^{11}B, due to its preferential affinity in the fluid released during the phase transition. The effect of B isotope fractionation associated with serpentine phase transition was modelled using the lizardite-fluid B isotope fractionation derived from the computational study of Li *et al.* (2022; B-lizardite-III_j structure), assuming B speciation in fluid is 100 % in tetrahedral coordination according to the alkaline condition of the serpentinite system during prograde subduction (*e.g.*, Debret and Sverjensky, 2017). Both batch and Rayleigh B isotope fractionations were modelled representing close *vs.* open evolution of the system, respectively. Calculations were done at 320 and 410 °C, overlapping the main T range of lizardite to antigorite transition during prograde subduction (Schwartz *et al.*, 2013) and the estimated T with antigorite-magnetite O isotope geothermometer (Debret *et al.*, 2019). Two cases were modelled based on different initial B contents and $\delta^{11}B$ signatures of the lizardite precursor. Values of 63 µg/g and +7 ‰ were adopted as representative of the M10 lizardite sample (highest and mean values, respectively; Fig. 3c in the main text),

whereas values of 81 µg/g and +20 ‰ were adopted as representative of the Conical serpentinites (values from Benton *et al.*, 2001; Fig. S-9). The latter is also used to test (i) how the variability in the initial [B] inventory and $\delta^{11}B$ signature of the lizardite and (ii) how the changes in B speciation in fluid in tetrahedral coordination from 100 % to 50 % may affect the results of the model.

Supplementary Tables

Table S-1 Sample information (modified from Debret *et al.*, 2019) and estimated pH-B composition of pore fluids where samples were collected (from Fryer *et al.*, 2018). TS: shipboard sample with thin section description available in Fryer *et al*. (2018).

Sample	Label identifier	Rock type	Nature of the embedding mud	Depth (m)	pH estimate	B in pore fluids (µM)
M10	366-U1493B-9X-CC-W 14/16	Liz-serpentinite (± Atg-Bru veins)	Large clast (>10 cm long) with no embedding mud	30.67	8.5	120
M12	366-U1495B-3G-CC-W 5/7	Transitional serpentinite (Liz + Atg)	Large clast (>10 cm long) with no embedding mud	4.84	9.2	450
M15	366-U1495B-6F-CC-W 10/12	Atg-serpentinite (+Bru)	Small clast (~2–5 cm long) with no embedding mud	10.71	11	500
M16 (TS63)	366-U1495A-3G-CC-W 13/15-TSB-TS_63	Atg-serpentinite (+Bru)	Small clast (~2–5 cm long) with no embedding mud	5.93	9.5	450
M20	366-U1496A-2F-4-W 12/14	Brucitite (± Serp)	Green serpentinite pebbly mud	6.2	12.5	1100
M24	366-U1496B-5F-1-W 77/82	Blue-serpentinite	Green serpentinite pebbly mud	16.77	12.5	1100

Table S-2 Boron isotope data of the Koh-OL olivine used as primary calibrating standard in two different analytical sessions. Reference $\delta^{11}B$ value of −4.6 ± 0.8 ‰ from Clarke *et al.* (2020). Boron content is estimated comparing the ^{11}B signal intensity between olivine and NIST 612 glass (see Analytical Methods).

# Analysis	B (µg/g)	$^{11}B/^{10}B$ measured	$^{11}B/^{10}B$ corrected	2 s.e.	$\delta^{11}B$ (‰)	2 s.e. (‰)
#1	72.2	4.5814	4.0241	0.0011	-4.82	0.26
#2	69.0	4.5824	4.0250	0.0011	-4.60	0.26
#3	64.7	4.5801	4.0230	0.0013	-5.10	0.31
#4	80.5	4.5837	4.0261	0.0011	-4.32	0.27
#5	79.4	4.5838	4.0263	0.0011	-4.29	0.27
#6	73.8	4.5828	4.0254	0.0011	-4.50	0.28
#7	90.5	4.5837	4.0252	0.0010	-4.56	0.24
#8	93.6	4.5844	4.0258	0.0010	-4.40	0.26
#9	82.5	4.5827	4.0243	0.0011	-4.77	0.28
#10	95.7	4.5832	4.0248	0.0012	-4.67	0.30
#11	95.7	4.5836	4.0253	0.0012	-4.53	0.31
#12	87.9	4.5832	4.0252	0.0012	-4.56	0.29
#13	73.4	4.5803	4.0254	0.0012	-4.50	0.30
#14	69.0	4.5791	4.0246	0.0011	-4.71	0.28
#15	65.5	4.5786	4.0244	0.0014	-4.75	0.34
#16	113.3	4.5849	4.0250	0.0008	-4.61	0.21
#17	112.0	4.5857	4.0258	0.0010	-4.41	0.25
#18	100.7	4.5846	4.0249	0.0010	-4.64	0.25
#19	110.9	4.5822	4.0247	0.0012	-4.68	0.30
#20	110.8	4.5824	4.0250	0.0011	-4.61	0.26
#21	104.7	4.5831	4.0258	0.0010	-4.41	0.26
#22	88.1	4.5802	4.0261	0.0012	-4.33	0.30
#23	79.0	4.5795	4.0256	0.0010	-4.45	0.25
#24	75.1	4.5787	4.0250	0.0012	-4.59	0.29
Mean	87.0	4.5823	4.0251		-4.58	
2 s.d.	31.4	0.0041	0.0015		0.36	

Table S-3 Boron isotope data of the MS VAR 10-01 antigorite used as quality control. Reference $\delta^{11}B$ value of +22.3 ± 0.4 ‰ from Cannaò *et al.* (2016).

# Analysis	B (µg/g)	$\delta^{11}B$ (‰)	2 s.e. (‰)
#1	15.4	+22.68	0.64
#2	17.4	+20.59	0.66
#3	13.3	+21.43	0.85
#4	14.8	+21.74	0.74
#5	15.0	+22.12	0.89
#6	16.7	+22.32	0.68
#7	18.6	+21.59	0.60
#8	14.6	+20.90	0.73
#9	14.5	+19.80	0.78
#10	16.3	+20.94	0.89
Mean	15.7	+21.41	
2 s.d.	3.2	1.74	

Table S-4 *In situ* trace element (µg/g) and $\delta^{11}B$ (‰) composition of serpentines from the Asùt Tesoru seamount. Trace elements were determined with LA-ICP-MS. Boron isotopes were measured with LA-MC-ICP-MS.

Table S-5 Boron isotope compositions of slab restite and slab-derived fluids together with lizardite in equilibrium with slab fluids at both alkaline and acid/neutral pH conditions of the system.

Table S-6 Geochemical parameters used to calculate the water/rock ratios. Concentrations are reported in ppm.

Table S-7 Rayleigh B isotope fractionation ($\Delta^{11}B$) between lizardite-fluids and olivine-lizardite (from Li *et al.*, 2022).

Tables S-4 to S-7 are available for download (.xlsx) from the online version of this article at http://doi.org/10.7185/geochemlet.2416.

Supplementary Figures

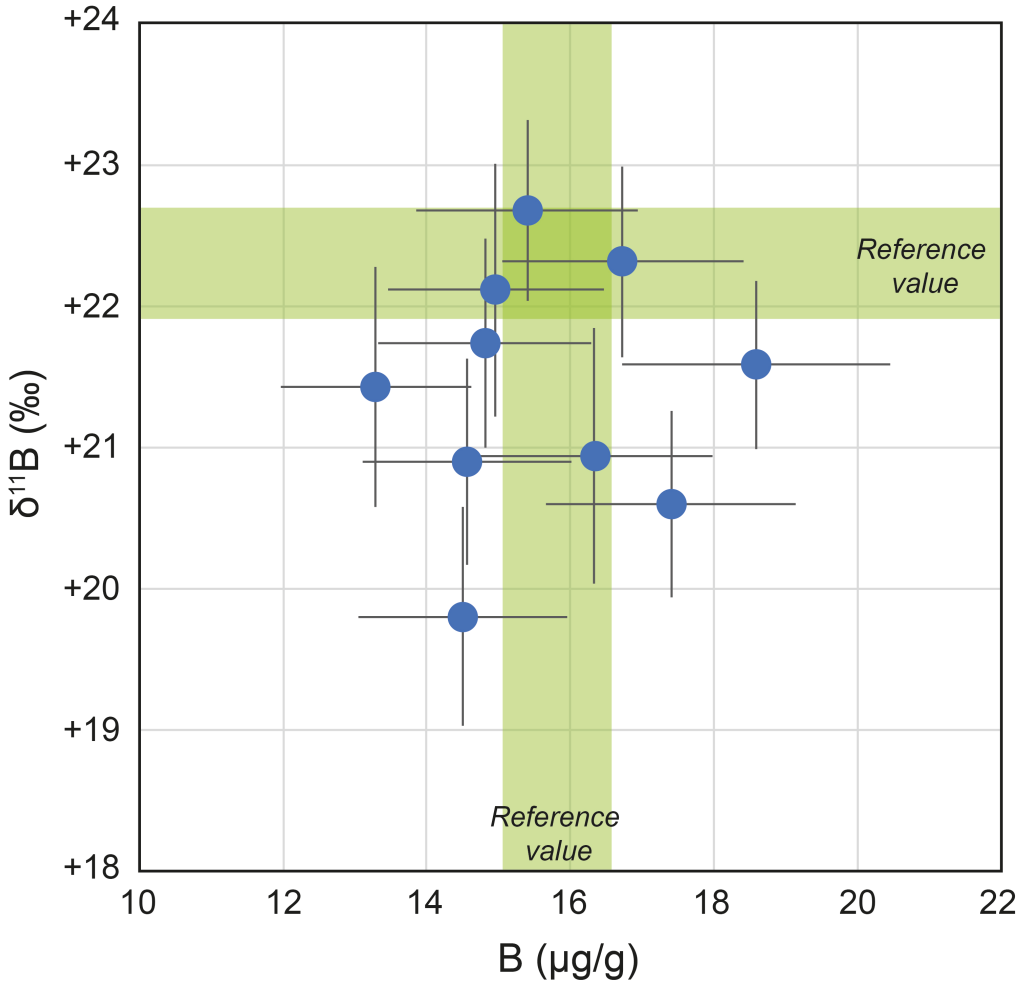

Figure S-1 B (µg/g) *vs.* δ^{11}B (‰) diagram of the MS VAR 10-01 antigorite measured as quality control. Error bars are 2 s.e. for δ^{11}B and estimated to be 15 % for B content (2 s.d.; see Cannaò *et al.*, 2024). Reference values are from Cannaò *et al.* (2016). Note that the δ^{11}B variability measured here for the MS VAR 10-01 antigorite is comparable with that of other reference antigorite used to correct for matrix effect at the Secondary Ion Mass Spectrometry (*e.g.*, Clarke *et al.*, 2020).

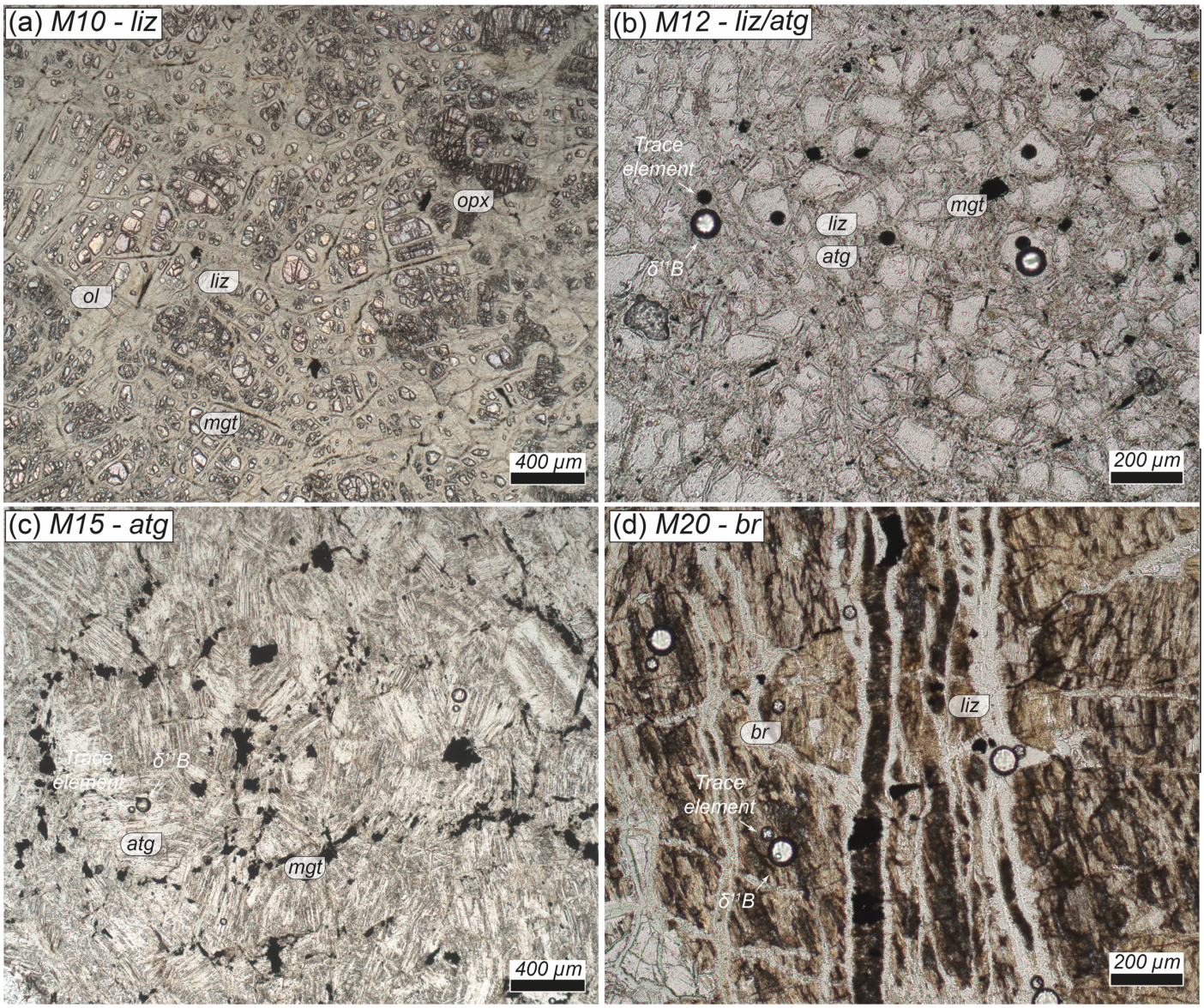

Figure S-2 Microphotographs of key samples from the Asùt-Tesoru seamount analysed in this study. **(a)** Lizardite-bearing sample (M10) showing lizardite (liz) replacing both olivine (ol) and orthopyroxene (opx) in mesh textures. Small isolated spinels and thin trails of magnetite (mgt) are visible. **(b)** Sample M12 showing lizardite replaced by antigorite (atg) along mesh texture. **(c)** Antigorite from sample M15 showing complex texture with abundant magnetite (see **(a)** for comparison). **(d)** Brucitite sample M20 made of brucite (br) partially overprinted by lizardite along major veinlets. Opaque phases in this sample are Fe-bearing hydroxides or sulfides (Debret *et al.*, 2019, 2022). Laser ablation spots from the trace element and B isotope sessions are also visible.

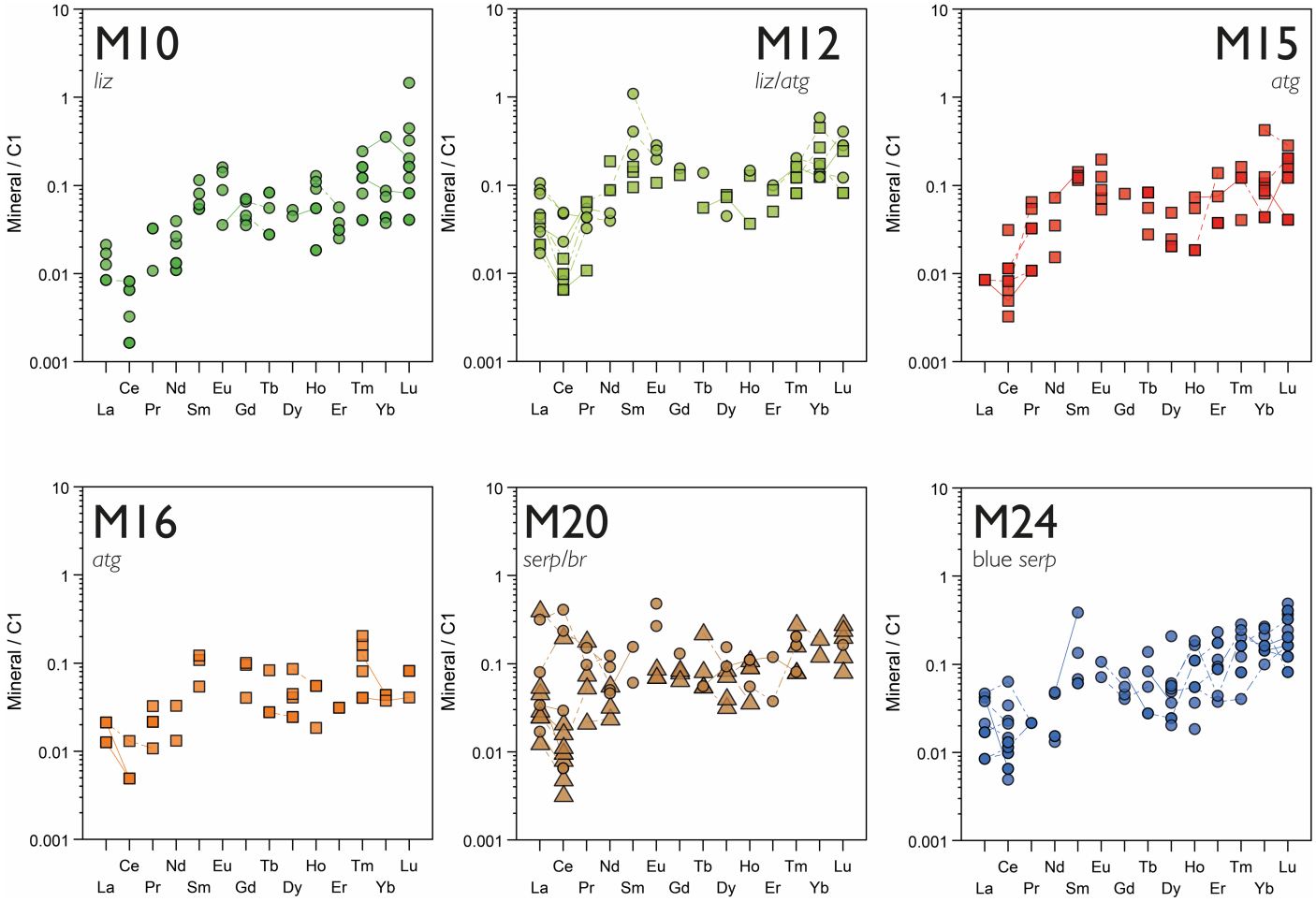

Figure S-3 Rare earth element patterns normalised to Chondrite (C1; McDonough and Sun, 1995) for the different Asùt Tesoru serpentinite samples. Circles, lizardite; squares, antigorite; triangles, brucite.

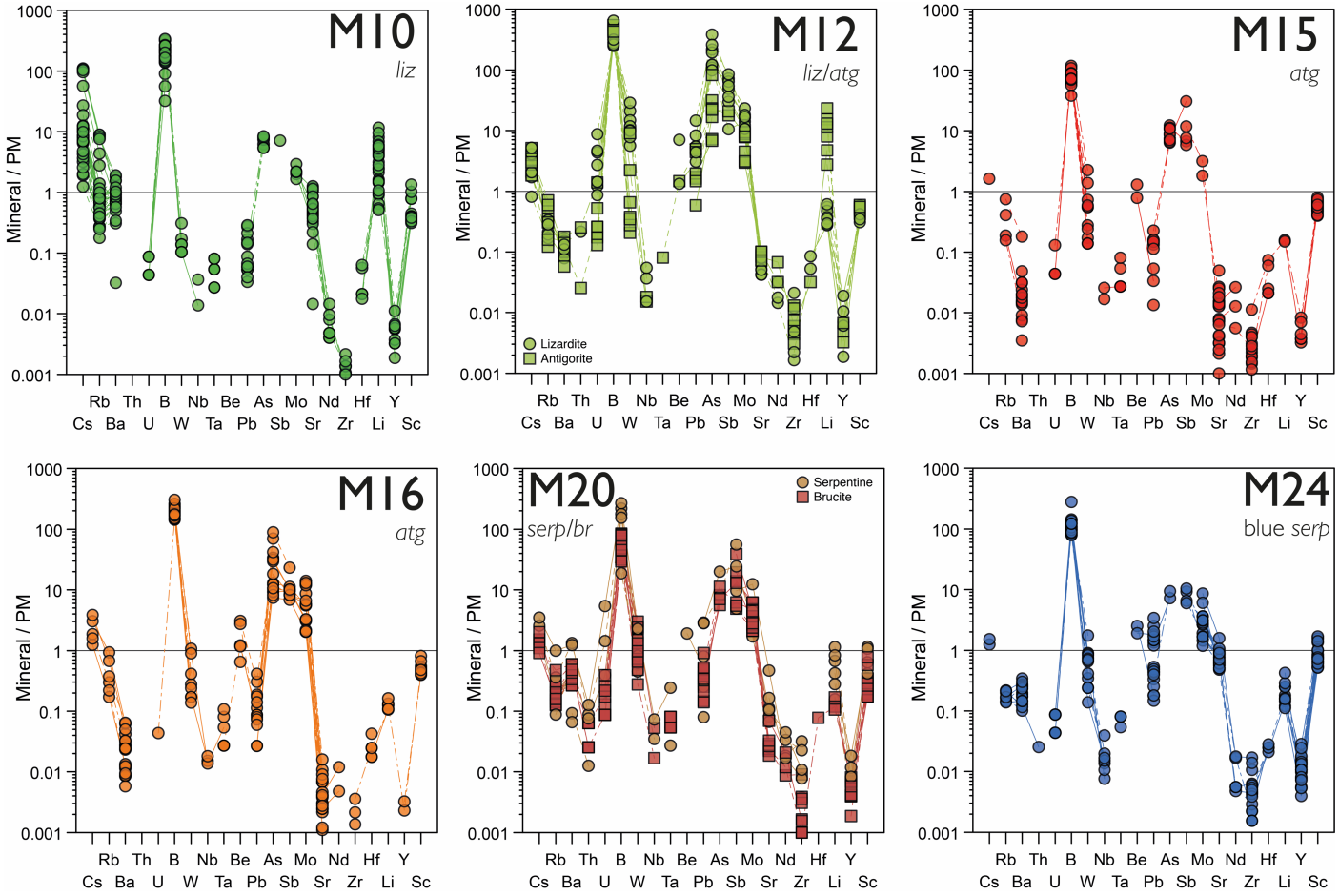

Figure S-4 Incompatible trace element spider diagrams normalised to the primitive mantle (PM; McDonough and Sun, 1995) for the different Asùt Tesoru serpentinite samples.

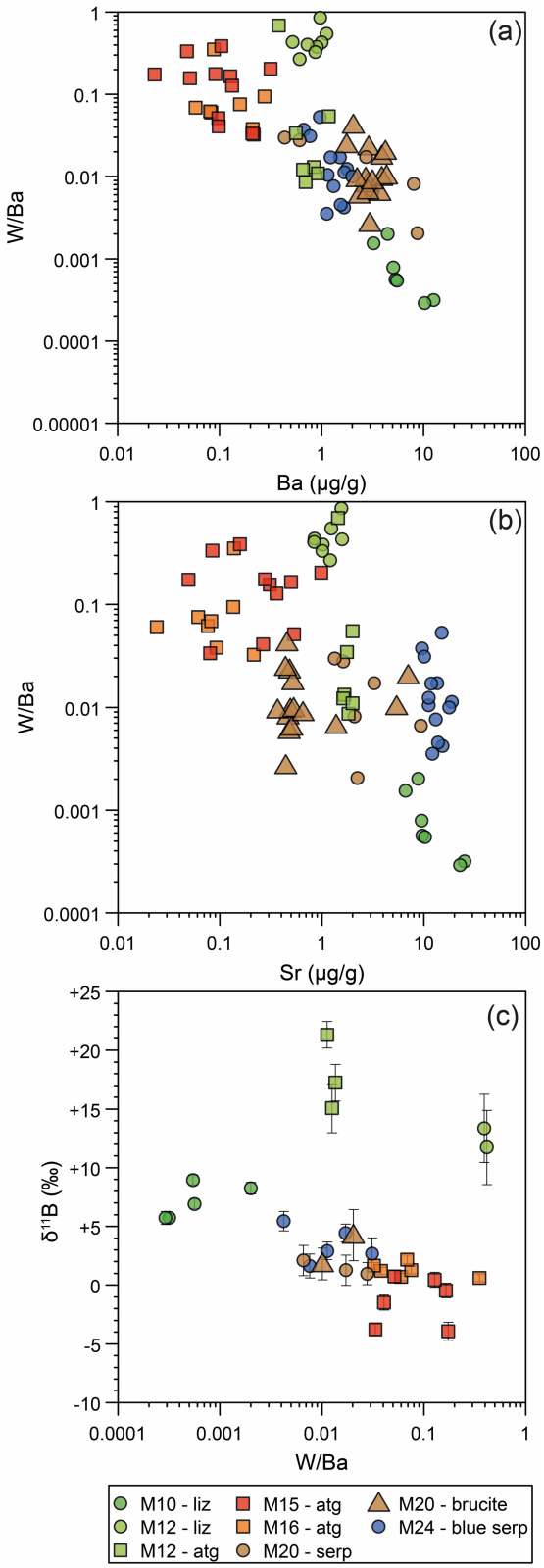

Figure S-5 Plots of trace element contents in serpentines for **(a)** Ba (µg/g) *vs.* W/Ba ratio and **(b)** Sr (µg/g) *vs.* W/Ba ratio. **(c)** Relationship between $\delta^{11}B$ (‰) and W/Ba ratio.

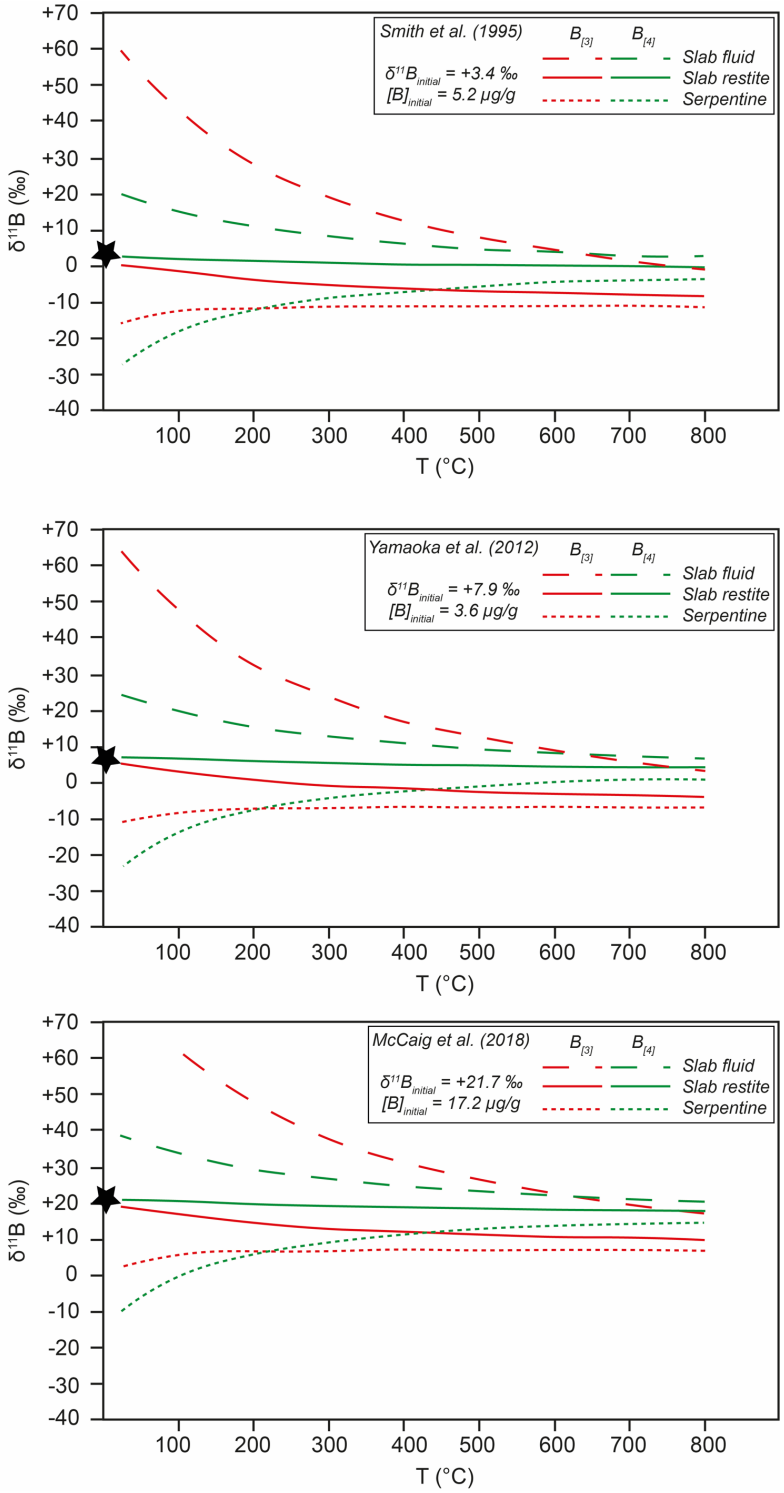

Figure S-6 Modelled B-isotope fractionation between slab-restite (solid lines), slab-fluid (coarse dashed lines) and serpentine (fine dashed lines) at acid/neutral (in red, [3]) and alkaline (in green, [4]) pH conditions of the system. The calculation assumes different starting composition of the slab input (black stars) as indicated in the boxes. Evolution of the serpentine B isotope signatures related to W/R ratios are reported in Figure S-7.

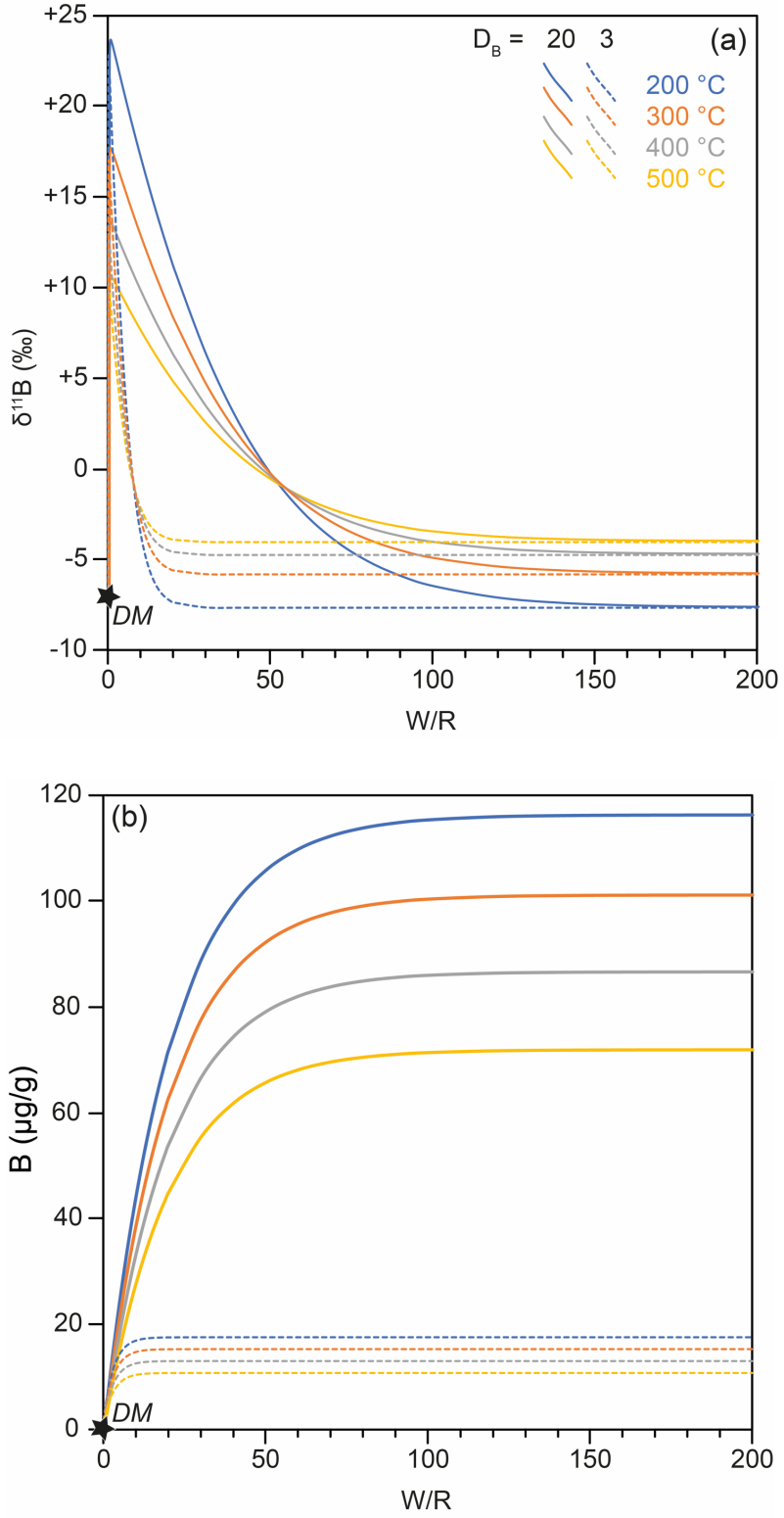

Figure S-7 Relations between W/R ratios and **(a)** $\delta^{11}B$ signatures and **(b)** B contents of the reacted rock (*i.e.* serpentinite) at different T (°C) and B partition coefficient (D_B). The calculation assumes mixed ([3–4]) B coordination in the system. Depleted mantle value (DM) form Marschall *et al.* (2017).

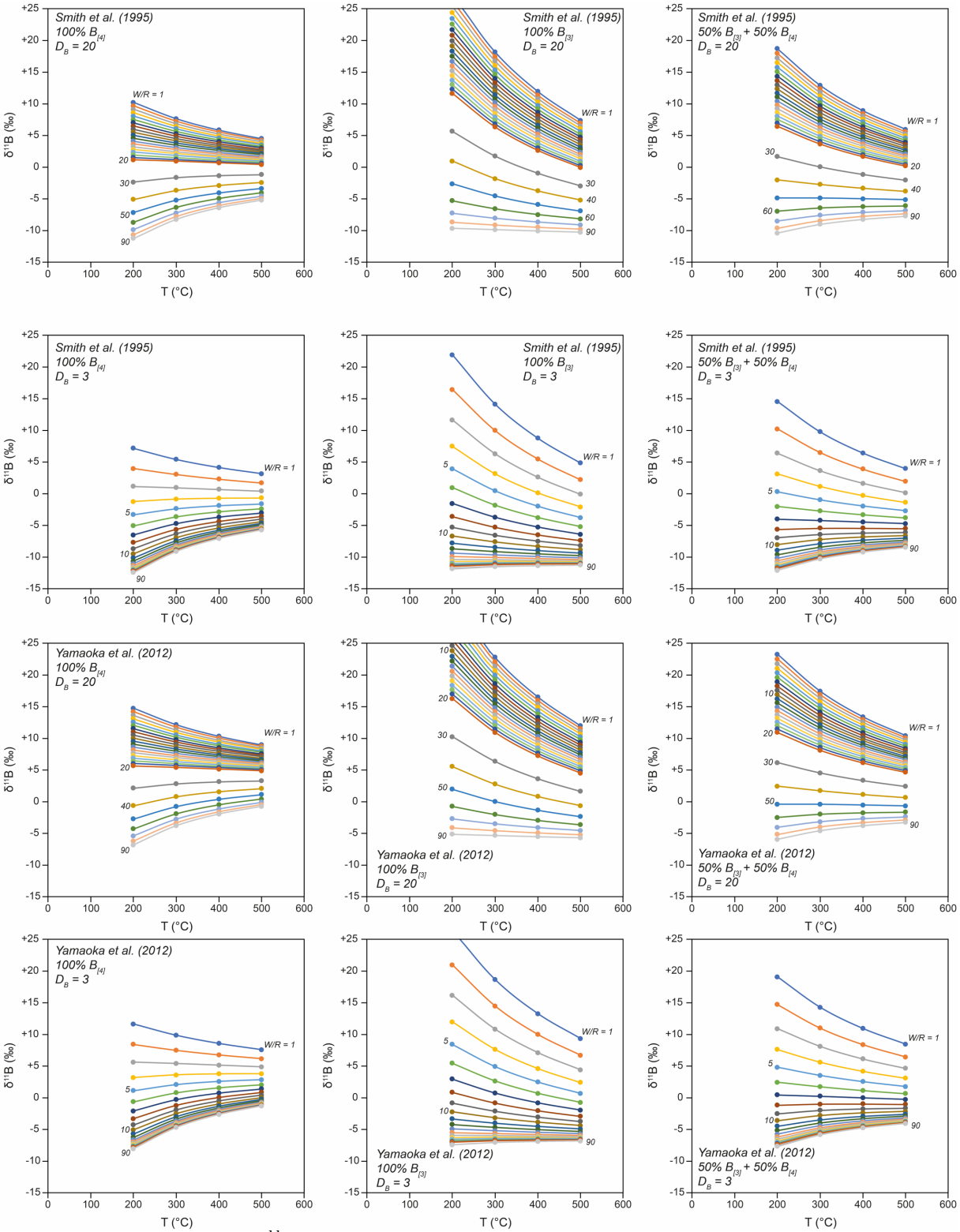

Figure S-8 Relations between $\delta^{11}B$ of serpentine and T (°C) for different water/rock ratios (W/R). The calculation assumes B in fluids in tetrahedral ([4]), trigonal ([3]) or mixed ([3–4]) coordination for B partition coefficient between serpentine and fluid (D_B) of 20 and 3 (see inset in each panel). The calculations are based on initial values of Smith *et al.* (1995) or Yamaoka *et al.* (2012). Positive $\delta^{11}B$ in serpentine can be achieved at low W/R ratios (*ca.* 1–5) at acidic or mixed conditions. If the pure alkaline endmember is considered, W/R ratios below 1 are required to form serpentine with $\delta^{11}B$ higher than *ca.* +10 ‰.

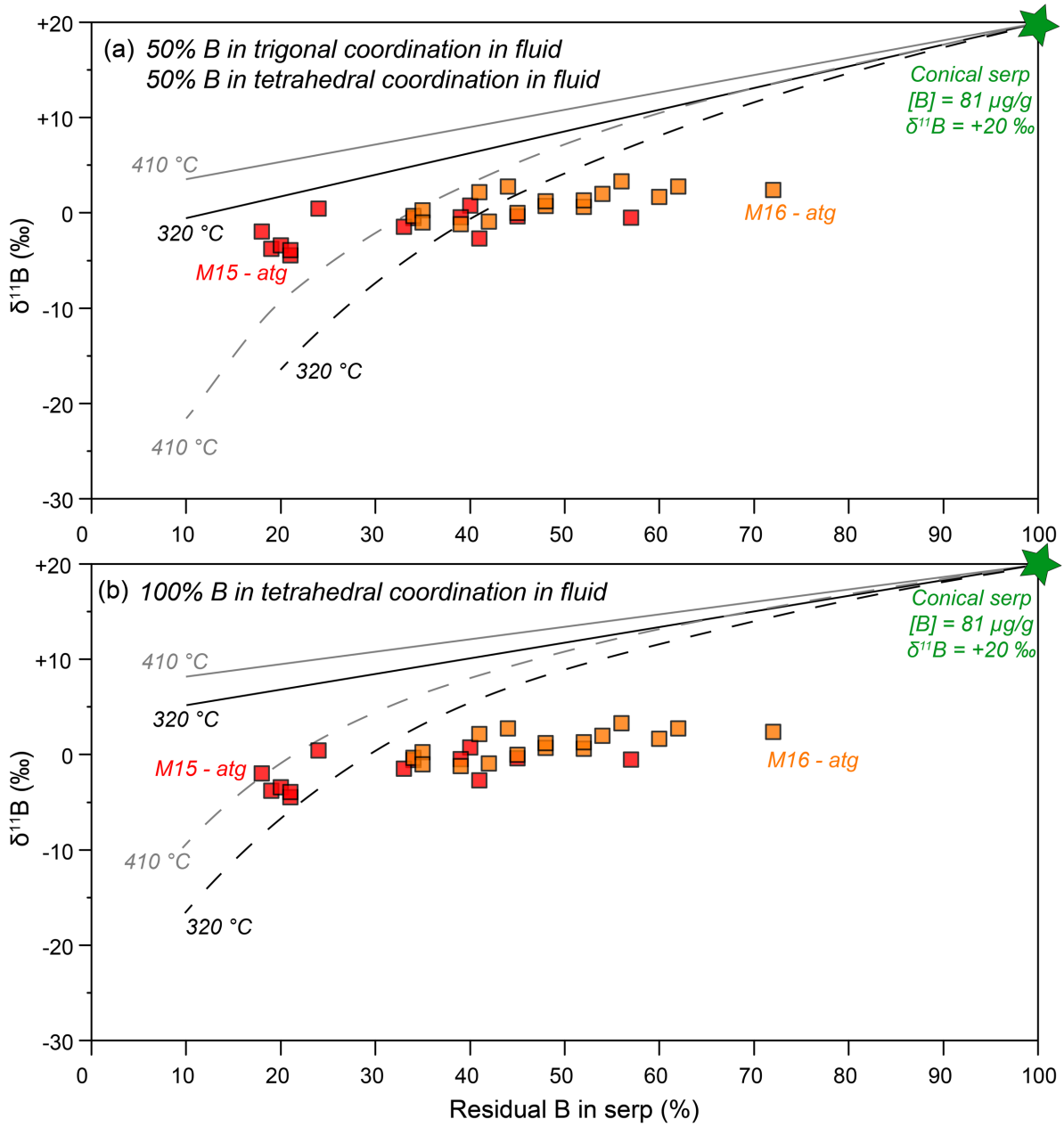

Figure S-9 Variations of [B] and $\delta^{11}B$ according to batch (solid lines) and Rayleigh (dashed lines) devolatilisation at 320 and 410 °C (black and grey, respectively) considering **(a)** 50 % to **(b)** 100 % alkaline condition of the system.

Supplementary Information References

Benton, L.D., Ryan, J.G., Tera, F. (2001) Boron isotope systematics of slab fluids as inferred from a serpentine seamount, Mariana forearc. *Earth and Planetary Science Letters* 187, 273–282. https://doi.org/10.1016/S0012-821X(01)00286-2

Bouilhol, P., Burg, J.-P., Bodinier, J.-L., Schmidt, M.W., Bernasconi, S.M., Dawood, H. (2012) Gem olivine and calcite mineralization precipitated from subduction-derived fluids in the Kohistan arc-mantle (Pakistan). *The Canadian Mineralogist* 50, 1291–1304. https://doi.org/10.3749/canmin.50.5.1291

Cannaò, E. (2020) Boron isotope fractionation in subducted serpentinites: A modelling attempt. *Lithos* 376–377, 105768. https://doi.org/10.1016/j.lithos.2020.105768

Cannaò, E., Scambelluri, M., Agostini, S., Tonarini, S., Godard, M. (2016) Linking serpentinite geochemistry with tectonic evolution at the subduction plate-interface: The Voltri Massif case study (Ligurian Western Alps, Italy). *Geochimica et Cosmochimica Acta* 190, 115–133. https://doi.org/10.1016/j.gca.2016.06.034

Cannaò, E., Scambelluri, M., Müntener, O., Putlitz, B., Agostini, S. (2023) Inheritance *versus* subduction-related $\delta^{11}B$ signatures of eclogites: Insights from the Voltri Massif (Ligurian Western Alps, Italy). *Chemical Geology* 615, 121218. https://doi.org/10.1016/j.chemgeo.2022.121218

Cannaò, E., Tiepolo, M., Agostini, S., Scambelluri, M. (2024) Fossil hydrothermal oceanic systems through *in-situ* B isotopes in ophicarbonates (N. Apennines, Italy). *Chemical Geology* 645, 121899. https://doi.org/10.1016/j.chemgeo.2023.121899

Catanzaro, E.J., Champion, C.E., Garner, E.L., Marinenko, G., Sappenfield, K.M., Shields, W.R. (1970) *Boric Acid: Isotopic and Assay Standard Reference Materials*. Special Publication 260-17, National Bureau of Standards, Washington, D.C. https://nvlpubs.nist.gov/nistpubs/Legacy/SP/nbsspecialpublication260-17.pdf

Clarke, E., De Hoog, J.C.M., Kirstein, L.A., Harvey, J., Debret, B. (2020) Metamorphic olivine records external fluid infiltration during serpentinite dehydration. *Geochemical Perspectives Letters* 16, 25–29. https://doi.org/10.7185/geochemlet.2039

Debret, B., Sverjensky, D.A. (2017) Highly oxidising fluids generated during serpentinite breakdown in subduction zones. *Scientific Reports* 7, 10351. https://doi.org/10.1038/s41598-017-09626-y

Debret, B., Albers, E., Walter, B., Price, R., Barnes, J.D., Beunon, H., Facq, S., Gillikin, D.P., Mattielli, N., Williams, H. (2019) Shallow forearc mantle dynamics and geochemistry: New insights from IODP Expedition 366. *Lithos* 326–327, 230–245. https://doi.org/10.1016/j.lithos.2018.10.038

Debret, B., Ménez, B., Walter, B., Bouquerel, H., Bouilhol, P., Mattielli, N., Pisapia, C., Rigaudier, T., Williams, H.M. (2022) High-pressure synthesis and storage of solid organic compounds in active subduction zones. *Science Advances* 8, eabo2397. https://doi.org/10.1126/sciadv.abo2397

Fietzke, J., Anagnostou, E. (2023) Sources of Inaccuracy in Boron Isotope Measurement Using LA-MC-ICP-MS. *Geostandards and Geoanalytical Research* 47, 481–492. https://doi.org/10.1111/ggr.12511

Foustoukos, D.I., Savov, I.P., Janecky, D.R. (2008) Chemical and isotopic constraints on water/rock interactions at the Lost City hydrothermal field, 30°N Mid-Atlantic Ridge. *Geochimica et Cosmochimica Acta* 72, 5457–5474. https://doi.org/10.1016/j.gca.2008.07.035

Fryer, P., Wheat, C.G., Williams, T., Expedition 366 Scientists (2018) *Mariana Convergent Margin and South Chamorro Seamount*. Proceedings of the International Ocean Discovery Program, Volume 366, College Station, TX. https://doi.org/10.14379/iodp.proc.366.2018

Hulme, S.M., Wheat, C.G., Fryer, P., Mottl, M.J. (2010) Pore water chemistry of the Mariana serpentinite mud volcanoes: A window to the seismogenic zone. *Geochemistry, Geophysics, Geosystems* 11, Q01X09. https://doi.org/10.1029/2009GC002674

Ingrin, J., Kovács, I., Deloule, E., Balan, E., Blanchard, M., Kohn, S.C., Hermann, J. (2014) Identification of hydrogen defects linked to boron substitution in synthetic forsterite and natural olivine. *American Mineralogist* 99, 2138–2141. https://doi.org/10.2138/am-2014-5049

Jochum, K.P., Weis, U., Stoll, B., Kuzmin, D., Yang, Q., Raczek, I., Jacob, D.E., Stracke, A., Birbaum, K., Frick, D.A., Günther, G., Enzweiler, J. (2011) Determination of Reference Values for NIST SRM 610–617 Glasses Following ISO Guidelines. *Geostandards and Geoanalytical Research* 35, 397–429. https://doi.org/10.1111/j.1751-908X.2011.00120.x

Kakihana, H., Kotaka, M., Satoh, S., Nomura, M., Okamoto, M. (1977) Fundamental Studies on the Ion-Exchange Separation of Boron Isotopes. *Bulletin of the Chemical Society of Japan* 50, 158–163. https://doi.org/10.1246/bcsj.50.158

Kimura, J.-I., Chang, Q., Ishikawa, T., Tsujimori, T. (2016) Influence of laser parameters on isotope fractionation and optimisation of lithium and boron isotope ratio measurements using laser ablation-multiple Faraday collector-inductively coupled plasma mass spectrometry. *Journal of Analytical Atomic Spectrometry* 31, 2305–2320. https://doi.org/10.1039/C6JA00283H

König, S., Münker, C., Schuth, S., Garbe-Schönberg, D. (2008) Mobility of tungsten in subduction zones. *Earth and Planetary Science Letters* 274, 82–92. https://doi.org/10.1016/j.epsl.2008.07.002

Kowalski, P.M., Wunder, B. (2018) Boron Isotope Fractionation Among Vapor–Liquids–Solids–Melts: Experiments and Atomistic Modeling. In: Marschall, H., Foster, G. (Eds.) *Boron Isotopes*. Springer, Cham, 33–69. https://doi.org/10.1007/978-3-319-64666-4_3

Kowalski, P.M., Wunder, B., Jahn, S. (2013) *Ab initio* prediction of equilibrium boron isotope fractionation between minerals and aqueous fluids at high *P* and *T*. *Geochimica et Cosmochimica Acta* 101, 285–301. https://doi.org/10.1016/j.gca.2012.10.007

Li, H.-Y., Zhao, R.-P., Li, J., Tamura, Y., Spencer, C., Stern, R.J., Ryan, J.G., Xu, Y.-G. (2021) Molybdenum isotopes unmask slab dehydration and melting beneath the Mariana arc. *Nature Communications* 12, 6015. https://doi.org/10.1038/s41467-021-26322-8

Li, Y.-C., Wei, H.-Z., Palmer, M.R., Jiang, S.-Y., Liu, X., Williams-Jones, A.E., Ma, J., Lu, J.-J., Lin, Y.-B., Dong, G. (2021) Boron coordination and B/Si ordering controls over equilibrium boron isotope fractionation among minerals, melts, and fluids. *Chemical Geology* 561, 120030. https://doi.org/10.1016/j.chemgeo.2020.120030

Li, Y.-C., Wei, H.-Z., Palmer, M.R., Ma, J., Jiang, S.-Y., Chen, Y.-X., Lu, J.-J., Liu, X. (2022) Equilibrium boron isotope fractionation during serpentinization and applications in understanding subduction zone processes. *Chemical Geology* 609, 121047. https://doi.org/10.1016/j.chemgeo.2022.121047

Liu, H., Xue, Y.-Y., Yang, T., Jin, X., You, C.-F., Lin, C.-T., Sun, W.-D., Deng, J. (2022) Fluid-rock interactions at shallow depths in subduction zone: Insights from trace elements and B isotopic composition of metabasites from the Mariana forearc. *Lithos* 422–423, 106730. https://doi.org/10.1016/j.lithos.2022.106730

Marschall, H.R., Altherr, R., Rüpke, L. (2007) Squeezing out the slab — modelling the release of Li, Be and B during progressive high-pressure metamorphism. *Chemical Geology* 239, 323–335. https://doi.org/10.1016/j.chemgeo.2006.08.008

Marschall, H.R., Wanless, V.D., Shimizu, N., Pogge von Strandmann, P.A.E., Elliott, T., Monteleone, B.D. (2017) The boron and lithium isotopic composition of mid-ocean ridge basalts and the mantle. *Geochimica et Cosmochimica Acta* 207, 102–138. https://doi.org/10.1016/j.gca.2017.03.028

McCaig, A.M., Titarenko, S.S., Savov, I.P., Cliff, R.A., Banks, D., Boyce, A., Agostini, S. (2018) No significant boron in the hydrated mantle of most subducting slabs. *Nature Communications* 9, 4602. https://doi.org/10.1038/s41467-018-07064-6

McDonough, W.F., Sun, S.-s. (1995) The composition of the Earth. *Chemical Geology* 120, 223–253. https://doi.org/10.1016/0009-2541(94)00140-4

Muir, J.M.R., Chen, Y., Liu, X., Zhang, F. (2022) Extremely Stable, Highly Conductive Boron-Hydrogen Complexes in Forsterite and Olivine. *Journal of Geophysical Research: Solid Earth* 127, e2022JB024299. https://doi.org/10.1029/2022JB024299

Pabst, S., Zack, T., Savov, I.P., Ludwig, T., Rost, D., Vicenzi, E.P. (2011) Evidence for boron incorporation into the serpentine crystal structure. *American Mineralogist* 96, 1112–1119. https://doi.org/10.2138/am.2011.3709

Pabst, S., Zack, T., Savov, I.P., Ludwig, T., Rost, D., Tonarini, S., Vicenzi, E.P. (2012) The fate of subducted oceanic slabs in the shallow mantle: Insights from boron isotopes and light element composition of metasomatized blueschists from the Mariana forearc. *Lithos* 132–133, 162–179. https://doi.org/10.1016/j.lithos.2011.11.010

Palmer, M.R., Swihart, G.H. (1996) Boron isotope geochemistry: an overview. *Reviews in Mineralogy* 33, 709–744. https://doi.org/10.1515/9781501509223-015

Palmer, M.R., London, D., Morgan VI, G.B., Babb, H.A. (1992) Experimental determination of fractionation of $^{11}B/^{10}B$ between tourmaline and aqueous vapor: A temperature- and pressure-dependent isotopic system. *Chemical Geology: Isotope Geoscience section* 101, 123–129. https://doi.org/10.1016/0009-2541(92)90209-N

Peacock, S.M., Hervig, R.L. (1999) Boron isotopic composition of subduction-zone metamorphic rocks. *Chemical Geology* 160, 281–290. https://doi.org/10.1016/S0009-2541(99)00103-5

Rosner, M., Erzinger, J., Franz, G., Trumbull, R.B. (2003) Slab-derived boron isotope signatures in arc volcanic rocks from the Central Andes and evidence for boron isotope fractionation during progressive slab dehydration. *Geochemistry, Geophysics, Geosystems* 4, 9005. https://doi.org/10.1029/2002GC000438

Scambelluri, M., Cannaò, E., Gilio, M. (2019) The water and fluid-mobile element cycles during serpentinite subduction: A review. *European Journal of Mineralogy* 31, 405–428. https://doi.org/10.1127/ejm/2019/0031-2842

Schwartz, S., Guillot, S., Reynard, B., Lafay, R., Debret, B., Nicollet, C., Lanari, P., Auzende, A.L. (2013) Pressure-temperature estimates of the lizardite/antigorite transition in high pressure serpentinites. *Lithos* 178, 197–210. https://doi.org/10.1016/j.lithos.2012.11.023

Seyfried Jr, W.E., Dibble Jr, W.E. (1980) Seawater-peridotite interaction at 300°C and 500 bars: implications for the origin of oceanic serpentinites. *Geochimica et Cosmochimica Acta* 44, 309–321. https://doi.org/10.1016/0016-7037(80)90139-8

Simon, L., Lécuyer, C., Putelat, T. (2016) The calculation of water-rock ratios using trace element (Li, B) stable isotopes. *Annales Universitatis Mariae Curie-Sklodowska, sectio AAA – Physica* 71, 79–89. https://doi.org/10.17951/aaa.2016.71.79

Smith, H.J., Spivack, A.J., Staudigel, H., Hart, S.R. (1995) The boron isotopic composition of altered oceanic crust. *Chemical Geology* 126, 119–135. https://doi.org/10.1016/0009-2541(95)00113-6

Spivack, A.J., Edmond, J.M. (1987) Boron isotope exchange between seawater and the oceanic crust. *Geochimica et Cosmochimica Acta* 51, 1033–1043. https://doi.org/10.1016/0016-7037(87)90198-0

Tonarini, S., Agostini, S., Doglioni, C., Innocenti, F., Manetti, P. (2007) Evidence for serpentinite fluid in convergent margin systems: The example of El Salvador (Central America) arc lavas. *Geochemistry, Geophysics, Geosystems* 8, Q09014. https://doi.org/10.1029/2006GC001508

Tonarini, S., Leeman, W.P., Leat, P.T. (2011) Subduction erosion of forearc mantle wedge implicated in the genesis of the South Sandwich Island (SSI) arc: Evidence from boron isotope systematics. *Earth and Planetary Science Letters* 301, 275–284. https://doi.org/10.1016/j.epsl.2010.11.008

Yamaoka, K., Ishikawa, T., Matsubaya, O., Ishiyama, D., Nagaishi, K., Hiroyasu, Y., Chiba, H., Kawahata, H. (2012) Boron and oxygen isotope systematics for a complete section of oceanic crustal rocks in the Oman ophiolite. *Geochimica et Cosmochimica Acta* 84, 543–559. https://doi.org/10.1016/j.gca.2012.01.043

Wilson, S. (2018) *G-probe 20 Summary Report*. International Association of Geoanalysts. https://www.geoanalyst.org/wp-content/uploads/2021/02/GP-20-report.pdf

Wu, S., Wörner, G., Jochum, K.P., Stoll, B., Simon, K., Kronz, A. (2019) The Preparation and Preliminary Characterisation of Three Synthetic Andesite Reference Glass Materials (ARM-1, ARM-2, ARM-3) for *In Situ* Microanalysis. *Geostandards and Geoanalytical Research* 43, 567–584. https://doi.org/10.1111/ggr.12301